This is a preproof accepted article for *Mineralogical Magazine*
This version may be subject to change during the production process
Doi: 10.1180/mgm.2025.30

Electrum dendrites from the Ametistovoe epithermal deposit, Kamchatka, Russia

Olga Yu. Plotinskaya[1,*], Vladimir V. Shilovskikh[2], Elena O. Groznova[3], Ludmila Yu. Kryuchkova[4], Reimar Seltmann[5]

[1] Institute of Geology of Ore Deposits, Petrography, Mineralogy and Geochemistry, Russian Academy of Sciences (IGEM RAS), Staromonetny per. 35, Moscow 119017, Russia

[2] St. Petersburg State University, Resource Center of Geoenvironmental Research & Modelling GEOMODEL, St. Petersburg 198504, Russia

[3] Institute of Experimental Mineralogy, Russian Academy of Sciences (IEM RAS), Chernogolovka, Moscow oblast', 142432, Russia

[4] St. Petersburg State University, Research Centre for X-ray Diffraction Studies, 199155, Dekabristov lane 16, St. Petersburg, Russia

[5] Natural History Museum, Department of Earth Science, Cromwell Rd, London SW7 5BD, UK

Submitted: November 1st, 2024

Abstract

Electrum dendrites and associated minerals from the Ametistovoe Au-Ag epithermal deposit (Kamchatka) were studied by optical and electron microscopy, X-ray computed tomography, electron microprobe and electron back scattered diffraction techniques. Electrum forms dendrites up to 1 mm in size within sphalerite, or, rarely, within galena and chalcopyrite and random particles within quartz. It has a very homogeneous chemical composition (fineness 603 to 615) which correlates neither with the host mineral nor with the electrum morphology. X-ray computed microtomography showed electrum dendrites are 2-dimensional and comprise acicular "trunk" hosting numerous "branches". 3-dimensional and "bush-like" dendrites are rare. Angles between "trunk" and "branches" are usually 90° and, less commonly, 60° suggesting twinning along (100) and (111) planes respectively. Electron back scattered diffraction evidenced the dendrites are single crystals with no defects detected while electrum within quartz has a mosaic texture with low pattern quality. A model proposed for the observed phenomena includes: 1) growth of single crystal electrum dendrites within silica gel; 2) overgrowth of dendrites by sphalerite crystals; 3) recrystallization of the opaline silica to crystalline quartz which resulted in destruction of electrum

* * Corresponding author. e-mail address: plotin@igem.ru

dendrites located within silica and preservation of those hosted by sphalerite. This model proposes crystallization of electrum dendrites from a hydrothermal solution and implied critical role of amorphous silica gel as a precursor for dendrites formation.

Keywords: electrum; dendrite formation; colloids; hydrothermal solutions; epithermal; Kamchatka

Introduction

Dendrites of electrum or, more rarely, of other ore minerals (galena, sphalerite, acanthite, naumannite, etc.) are common in bonanza ores of low-sulfidation epithermal Au-Ag deposits, as was recently reviewed by Tharalson et al. (2023). The most common explanation of dendrites formation is transport of gold nanoparticles by hydrothermal fluid and its subsequent deposition through aggregation simultaneously to the deposition of the silica colloids (Lindgren, 1915; Boydell, 1925; Frondel, 1938; Chukhrov, 1955; Betekhtin et al., 1958; Saunders, 1990; Saunders and Burke, 2017 and references therein). However, despite quite a good number of publications on gold dendrites very few attempts have been made to study their internal structure. Petrovskaya (1973) classified morphological varieties of gold dendrites and revealed mosaic texture in some of them; Saunders and Schoenly (1995) showed fractal nature of gold dendrites. Electrum surface has been investigated with high-resolution Scanning Electron Microscopy (SEM) (Borisova, 2010; Saunders et al., 2019; Monecke et al., 2023) but no attempt has been made to investigate the 3-dimensional morphology of dendrites, neither has their internal structure been studied with the exception of Burke et al. (2017) who studied gold dendrites with Transmission Electron Microscopy (TEM). It should be also noted that there is no precise definition of dendrites; they are commonly defined as tree-like morphology with no reference to internal structure. The latter helps to reveal the mechanisms of dendrites growth and may give a clue to understanding processes of deposition of bonanza ores.

In the last few years electron back-scattered diffraction (EBSD) has been proved as an effective tool to investigate micro- to nanoscale internal structure of minerals (Schwartz et al., 2009). This is of critical importance for cubic minerals, where internal structure, such as twinning, recrystallization, etc. cannot be revealed by optical microscopy. In particular, EBSD was successfully applied to natural native gold (Grimshaw et al., 2017; Butt et al., 2020; Chapman et al., 2021; Kozin et al., 2023; Palyanova et al., 2023) its synthetic analogues (Jhabvala et al., 2011, Bauer et al., 2020), and even to archaeological gold (Northover and Northover, 2012). This article presents the results of a comprehensive study of electrum dendrites and associated minerals from the Ametistovoe Au-

Ag epithermal deposit (Kamchatka) and focuses on internal structure and regularities of electrum dendrites growth. The approach includes study of fluid inclusions in co-existing minerals, X-ray computed tomography, electron microprobe and EBSD study.

Brief outline of geology and mineralogy of the Ametistovoe Au-Ag epithermal deposit

The Ametistovoe Au-Ag epithermal deposit is located in the northern part of the Kamchatka peninsula (Fig. 1a), ca. 100 km Northwest from the Korf settlement. The Kamchatka peninsula, representing the northernmost part of the Pacific Rim, hosts dozens of epithermal Au deposits and occurrences which are confined to three volcanic belts (Litvinov et al., 2019; Petrenko, 1999): Koryak-Western Kamchatka (submarine volcanics of Eocene-Oligocene age), Central Kamchatka (Oligocene to Quaternary rhyolite, dacite, andesite, basalt volcanics), and Eastern Kamchatka (basalts of Pliocene to Quaternary age). The Ametistovoe deposit is located in the northern part of the Central Kamchatka volcanic belt (Fig. 1a).

The deposit was discovered in 1967 by 1:200 000 scale geological survey; prospecting and exploration started in the 1970s and lasted to 1995. Ametistovoe has been exploited since 2012 by open pit and since 2019 by underground mining (http://zolkam.ru). Proven reserves for 2021 are ca. 34.4 tons of Au and ca. 106 tons of Ag (https://nedradv.ru/nedradv/ru/places). The Ametistovoe orefield is confined to the central part of the Tklavayam caldera composed of Oligocene volcanic sequence and subvolcanic bodies (Figs. 1b,c). The bottom of the sequence, up to 20m thick, represents rhyolite, rhyolite-dacite and felsic tuff with interlayers of tuffstone and coal typical for a deep caldera lake. The upper part is composed of dacite, andesite-dacite, andesite, andesite-basalt lava and tuff with a total thickness of 200 to 400m. Numerous subvolcanic diorite, andesite, and dacite porphyry stocks mark the main and subordinate vents. The Ametistovoe ore field, ca. 35 km^2, comprises ca. 300 steeply dipping quartz and kaolinite-quartz veins; the largest ones reach hundreds of meters in strike and are up to several meters thick. Veins are joined in bunches and ore zones which extend up to 1.5 km. Ore textures include massive, veinlet-disseminated, crustiform features. Sulfides are abundant and make up 3-5 to 30-50 vol.% of ore. Wall-rock alteration is represented by vuggy silica, quartz-kaolinite, kaolinite-hydromica-quartz, carbonate chlorite-quartz (Vartanyan et al., 1988). Nekrasov (1996) referred this alteration to argillic type.

Vartanyan et al. (1988) proposed four distinct stages:

I- pyrite-quartz (pyrite, arsenopyrite, minor magnetite, rutile, chlorite, hydromica, etc.);

II- sulfide-quartz (quartz, sphalerite, chalcopyrite, galena, pyrite, minor pyrrhotite, marcasite, stannite, scheelite, native gold, calcite, albite, etc.);

III- gold-kaolinite-chlorite- sulfide-quartz or the main ore stage (quartz, kaolinite, chlorite, pyrite, galena, sphalerite, native gold (electrum), acanthite, minor adularia, hydromica, dickite, calcite, tetrahedrite-group, naumannite, Ag sulfosalts, etc.);

IV- carbonate-quartz (quartz, calcite, stibnite, cinnabar, etc.).

Native gold fineness varies from 960 in early generation to 220 in late generation (Nekrasov, 1996) but most values are within 500-730 (Petrenko, 1999).

Previous researchers have classified the deposit as a low sulphidation or adularia-sericite type deposit (Vartanyan et al., 1988; Petrenko, 1999; Bortnikov and Tolstykh, 2023), but given its relation to the volcanic caldera, alteration type and abundance of sulfides, perhaps it is more akin to intermediate sulphidation type in the classification of Sillitoe and Hedenquist (2003).

Methods

SEM-EDX and Electron microprobe analysis

Ore and gangue minerals were analyzed with a Jeol-5900 SEM with Oxford instruments EDX detector (Natural History Museum, London). Electron microprobe analysis (EMPA) of electrum and sphalerite was performed with a Cameca SX-100 microprobe (NHM, London) equipped with five wavelength-dispersive X-ray detectors (WDX). For the following conditions were used: accelerating voltage 20 keV, sample current 20 nA, beam diameter 2 µm. For electrum signals used: *Kα* for S, Cu, As, Se, Ag, Sb, Te, Au, Hg and *Mα* for Pb and Bi. For sphalerite signals used: *Kα* for S, Cu, Fe, Zn, and Mn, *Lα* for Cd, standards: ZnS for S and Zn, CdS for Cd and pure metals for Mn, Fe, and Cu.

Fluid inclusion study

Microthermometric measurements of fluid inclusions were carried out on doubly polished thin sections using a LINKAM THM-600 heating-freezing stage in the Institute of Experimental Mineralogy Russian Academy of Sciences, Chernogolovka. The temperature of phase transitions was measured within the range –196 to +600°C with an accuracy of ±0.2°C between –20 and +20°C and no less than ±1.0°C outside of this interval. The salt composition of the fluids was determined from the eutectic temperature (T_e) according to Crawford (1981); the salinity was estimated from the temperature of ice melting (T_m) using the NaCl–H_2O phase diagram (Bodnar and Vityk, 1994). The measurements were carried out for groups of inclusions with similar relationships of phases to avoid errors related to the disintegration of vacuoles after fluid heterogenization (Roedder, 1984).

X-ray computed microtomography

Four cylinders with a diameter of ca. 2 to 2.5 mm were drilled from polished sections. The cylinders were scanned via an X-ray tomography analysis facility at the Centre for X-ray Diffraction Studies of the Research Park of St. Petersburg State University (analyst: L.Yu. Kryuchkova) using a SkyScan-1172 microtomography scanner (Bruker microCT, Belgium). The equipment settings were: accelerating voltage 100 keV; a current of 100 µA, an acquisition time of 3.8 to 5 sec per image, and 5 to 10 frames. An Al+Cu filter was used to minimize the hardening of the X-ray beam. Samples were scanned with rotation of 180 and 360°. To reconstruct the array of shadow images, NRecon software (Bruker microCT) was used, which allows leveling instrument artifacts and setting the range of gray gradations corresponding to the value of x-ray absorption and, accordingly, x-ray density. To analyze the obtained microtomographic data, DataViewer and CTVox software (Bruker microCT) were used.

Electron backscattered diffraction (EBSD)

All samples were treated with Ar plasma via Oxford IonFab300 plasma etcher (10 min exposure, 500 V accelerating voltage and 200 mA beam current) at the 'Nanophotonics' centre of SPbU, (Saint-Petersburg University, Russia). The electron back-scatter diffraction study was carried out with a Hitachi S-3400N electron microscope equipped with Oxford NordlysNano EBSD detector and energy dispersive spectrometer (EDS) Oxford X-Max 20 at the SPbU, 'Geomodel' centre (Saint-Petersburg, Russia). Operating conditions were: 30 kV (accelerating voltage), 2 to 5 nA (beam current), 4x4 pixels binning, averaging 2-3 images and total dwell time 30-60 µs per pixel. The obtained images were indexed automatically in real time based on quartz (P3221) and native gold (Fm3m) due to high probability of misindexing for native gold/galena/sphalerite/chalcopyrite. Subsequently cubic phases were separated manually based on element maps obtained by EDS. Data was processed with Oxford Channel5 software. Phase maps, band contrast (pattern quality) maps, inverse pole figures (IPF) maps and misorientation measurements were generated (Prior et al., 1999; Maitlan, and Sitzman, 2007; Brodusch et al., 2018 and references therein). The band contrast maps show the intensity of diffraction patterns, revealing the distribution of grain boundaries, twin boundaries, and microstructures within crystals. Grains with higher quality of diffraction pattern are colored by light gray, while ones with low quality are darker. Orientation data is represented in inverse polar figure (IPF) color schemes, which depicts coincidence of sample coordinate axis with crystal's orientation. This color scheme was chosen as more visual compared to universal ones. The

choice of exact sample coordinate axis is conditioned by higher visual contrast for reader's convenience.

Results

Mineral assemblages and composition

The available sample collection comprised 14 specimen of quartz-sulfide veins from Ametistovoe representing all four formation stages. For detailed investigation the sample which was visually most enriched in electrum was selected. The investigated sample represents mineralization of the gold-sulfide-kaolinite-chlorite-sulfide-quartz (main ore) stage. Several polished sections and two double-polished sections were prepared. In the studied sections the main ore stage is represented by aggregates of quartz and reddish-brown sphalerite (Fig. 2). Pyrite, chalcopyrite, galena and electrum are also common.

The mineral sequence observed in successive vein filling is as follows (Fig. 2a):

Most part of a vein is composed of microcrystalline quartz and sphalerite-1. Sphalerite forms crystals 1-2 mm and contains small inclusions of galena-1 and chalcopyrite-1 (Figs. 2b,c). Quartz, sphalerite-1, and, sometimes, galena-1 and chalcopyrite-1 contain abundant inclusions of electrum, mainly 10 to 40-50 μm in size (Fig. 2c). Within quartz electrum forms xenomorphic grains of irregular shape. In reflected light within sphalerite and other sulfides electrum has regular rounded or oval shapes, sometimes elongated up to 500 μm (Figs. 2d,f). In transmitted light, however, electrum appears to form dendrites within sphalerite (Figs. 2e,g). Rare hessite and Au-Ag tellurides, which could not be identified due to small size, were found in intergrowths with electrum.

Aggregate of electrum-bearing quartz and sulfides is overgrown by transparent quartz druse with idiomorphic transparent-white crystals followed by pyrite, sphalerite-2, chalcopyrite-2, and galena-2 (Figs. 2b,h). Sometimes these late sulfides also fill cracks in sphalerite-1. No electrum was observed here. Axial part of vein is filled with quartz-3 and minor chlorite (Fig. 2a,b).

Electrum exhibits a general uniform chemical composition (Table 1 and Supplement ESM 1): Au from 60.88 to 62.58 wt. %, Ag from 38.94 to 39.78 wt. %, Hg from 0.25 to 0.46 wt. % which corresponds to fineness of 603 to 615. No correlation between chemical composition and hosting mineral was noted. Sphalerite contains 2 to 8.15 wt. % of Fe (3.5 to 14.2 mol.% FeS), EMPA analysis revealed up to 0.13 wt. % Cu, up to 0.18 wt. % Mn and 0.22 to 0.28 wt. % of Cd (Table 2). Sphalerite-1 intergrown with electrum has 4.7 to 8.8, mean 6.3 mol.% FeS. It establishes chemical zonation (Fig. 2 d,f): core with 7.4 to 8.2 mol.% FeS and rim with ca. 4.7 mol.% FeS. Sphalerite-2 is featured by

chalcopyrite emulsion and has 3.5 to 14.2, mean 8.1 mol.% FeS (Table 2 and Supplement ESM 1). Chlorite (Table 3) belongs to clinochlore-daphnite series with insignificant amounts of sudoite (Bailey, 1988); X(Mg) makes up 0.36-0.37, the Si/Al ratio varies from 1.33 to 1.53. MnO is always present (1.43–1.72 wt.%), no Ti, Cr, Ca, Na, and K were detected. Chlorite formation temperatures were calculated according to (Cathelineau 1988; Kranidiotis and McLean, 1987; Kotelnikov et al., 2012) and all lie between 201°C and 273°C (Table 3).

Fluid inclusion data

Fluid inclusions (FI) were observed in quartz-2 and in electrum-bearing sphalerite-1. In quartz, FIs are confined to central parts of crystals; in sphalerite they are randomly scattered. For microthermometric study we selected FIs closest to electrum. All FIs are considered to be primary according to the criteria proposed by Roedder (1984). At room temperature all FIs have oval shape and are up to 20 μm in size; they consist of aqueous liquid and vapor bubbles (ca. 20 vol.%). No daughter minerals or trapped solids were observed.

All FIs studied homogenize into liquid phase upon heating. The results of a microthermometric study are presented in Table 4 and Figure 3. Fluid inclusions in quartz-2 show low salinities (4.2 to 6 wt.% NaCl equiv.) and eutectic temperatures (T_{eut}) of –23.7 to –25.8°C indicating that NaCl is dominant. They homogenize upon heating at 205 to 245°C. Fluid inclusions in sphalerite-1 are even more diluted (0.9 to 1.7 wt.% NaCl equiv.) and also are NaCl dominant (T_{eut} makes up –23.7 to –25.8°C). Homogenization temperature of FIs in sphalerite ranges 230 to 255°C.

Since no boiling or CO_2 effervescence was documented, the estimates of T_{hom} can be regarded as minimum trapping temperatures (Roedder, 1984). There is no reliable pressure estimate for the Ametistovoe deposit but taking into account its epithermal features the maximum depth of ore deposition did not exceed 1-1.5 km (Simmons et al., 2005 and references therein). i.e. maximum pressure for hydrostatic environment was ca. 100 bar. Pressure corrections for the homogenization temperatures (Potter, 1977) will, in this case, increase the temperature estimate by no more than 10–15°C, to between 220 – 260°C in quartz and to 245 – 270°C in sphalerite. Both pressure-corrected and non-corrected T_{hom} intervals overlap with the temperature estimates obtained for chlorite (Table 3). Similar homogenization temperature was also obtained earlier for gold-sulfide-chlorite quartz stage by A.G. Granovsky (1993).

X-ray computed microtomography

X-ray computed microtomography was carried out for four cylinders drilled from two polished sections. It confirmed dendritic morphology of electrum within sphalerite (Figs. 4a,b). Electrum dendrites are distributed relatively homogenously; their size rarely exceeds 1 mm. They comprise relatively long acicular "trunk" and numerous "branches" which are much shorter; "branches" of the second order are rare and small. Most branches develop in one plane making 2-dimensional dendrites. Angles between "trunk" and "branches" are usually 90° and, less commonly, 60° (Figs. 4c). In addition, single "bush-like" dendrites were noted; they comprise several (usually three to five) "branches" growing from one point (Figs. 4 d,e). No dendrites were found within quartz, despite electrum particles are abundant in quartz and often form clusters they do not show any regular distribution.

Electron backscattered diffraction (EBSD)

EBSD patterns were obtained for sites containing electrum and, where possible, maximum variability of hosting minerals, i.e., sphalerite, quartz, galena and sphalerite (Figs. 5, 6 and 7).

Sulfides

Sphalerite-1 has a high EBSD pattern quality (Fig. 5a,b) and comprises large randomly oriented grains with polysynthetic twinning (Figs. 5c). Galena-1 and chalcopyrite-1 also forms well crystallized randomly oriented grains (ESM 3).

Quartz

Quartz-1 that hosts electrum particles and is intergrown with electrum-bearing sphalerite has globular morphology (Figs. 5d-f, 6b-d) forming globules of 50 to 200 μm in diameter. In band contrast images these globules establish either microcrystalline jigsaw texture (Fig. 5e,f) or radial fibers (Fig.6c,d). The both varieties of globules coexist (Figs. 5f and 6d,e) which suggests globules with jigsaw texture are upper sections of radial globules. On IPF maps (Fig. 5f and 6b,e) most of quartz globules establish radial twinning structure with three segments with one crystallographic orientation and the other three with another; the orientation angle between twins is 60°. Twin boundaries are sometimes straight but often jugged (Fig. 6b, marked by arrows).

Electrum

Electrum particles located in quartz or on quartz/sphalerite boundaries show low quality of EBSD patterns (Fig. 5b) and are randomly oriented, as can be seen on IPF maps (Fig. 5d,e). Electrum

within sphalerite, in contrast, has much higher EBSD pattern quality, i.e. contains less lattice defects than those in quartz. On IPF maps (Figs. 5d,g) it forms clusters where several (three to dozen) grains have the same color, i.e. have the same crystallographic orientation. Each such cluster corresponds to a dendrite where “branches” grow on the “trunk” at the right angles, i.e. self-epitaxy on (100) plane. It is notable that one dendrite (group of electrum grains with the same orientation) can grow within both sphalerite and galena (Fig. 7). Rarely misorientation angle of 60° between “branch” and “trunk” was noted (Figs. 6e,f) suggesting self-epitaxy on (111) plane. Sometimes also minor misorientation within electrum grains can be observed (Figs. 6g,h).

Discussion

It was noted endogenic electrum dendrites are found mainly in ores of low-sulfidation epithermal Au-Ag deposits (Petrovskaya, 1973; Saunders and Burke, 2017; Tharalson et al., 2023 and references therein). Most authors link their formation with rapid crystallization (Lindgren, 1915; Ramdohr, 1969 etc.) which is common in near-surface epithermal environment. Usually gold dendrites occur within chalcedony-like silica; sometimes dendrites of tellurides, selenides, and sulfides were also described (Tharalson et al., 2023 and references therein). Gold or electrum dendrites within sphalerite and other sulfide minerals have not been previously documented.

Morphology of electrum dendrites

Petrovskaya (1973) reviewed gold dendrites from several deposits worldwide and noted most dendrites have a relatively long acicular “trunk” and much shorter “branches”. “Branches” may form 90 and 60 angles with the “trunk” overgrowing on (100) or (111) planes respectively. She also noted 3-dimensional (3-D) dendrites with branches growing in 3 mutually perpendicular directions and 2-dimensional (2-D) dendrites which often coexist but 2-D ones (or planar dendrites) dominate in nature. 1-D crystals with poorly developed or non-developed “branches” are also common. Saunders and Burke (2017) described planar dendritic crystals of native silver with a reticulate shape (90 angles between trunk and branches) which were encrusted by irregular "fractal" 3-D dendrites. These authors supposed the “reticulate” dendrites were formed from solutions by direct rapid chemical precipitation while "fractal" dendrites were formed by the random aggregation of gold nanoparticles. Synthetic dendrites (Yuan et al, 2004; Bauer et al., 2020 and references therein) show even more variable morphology. E.g. Bauer et al. (2020) obtained five-pointed star structures. However, trunks with branches with (100) and/or (111) epitaxy are also

most common. These observations are in a good agreement with features described in the present study (Fig. 4).

Chemical composition of electrum

The obtained microprobe data establish very homogeneous composition of electrum dendrites (fineness is mostly 600-620). Low fineness is rather typical for hypogene dendritic native gold, e.g. Petrovskaya (1973) noted Ag contents in dendrites higher than 25 wt.% (i.e. fineness less than 750). Tharalson et al. (2023) published a wider range of 428 to 963 for dendrites from four low sulfidation epithermal deposits from California and Nevada but most values fit within 540-780. However, native gold from epithermal deposits worldwide is featured by grain-scale, sample-scale, and deposit-scale variations in chemical composition, regardless its morphology (Petrovskaya, 1973; Morrison et al., 1991; Liu and Beaudoin, 2021; Tharalson et al., 2023). Thus, the observed chemical homogeneity of electrum dendrites from the Ametistovoe deposit is apparently anomalous and merits additional explanation.

Electrum, sphalerite, and quartz formation conditions

Electrum

Composition of Au-Ag alloy is known to be sensitive to physico-chemical conditions, i.e. temperature, pH, oxygen and sulfur fugacity (Barton and Toulmin, 1964; Shikazono, 1985; Palyanova, 2008; Liang and Hoshino, 2015). Rapid changes of any of these parameters due to boiling, cooling, fluids mixing, etc. would result in variability in electrum composition. However, colloidal gold (and silver) particles formed in different parts of vein and transported by the ascending fluid also would be variable in composition as well as the subsequently deposited dendrites or other electrum morphologies. For example, Novgorodova (2005) described variations in Ag contents up to 20 wt.% within blocks of metacolloidal (i.e. recrystallized colloidal) native gold from the Baley epithermal deposit. Petrovskaya et al. (1977) revealed via etching mosaic texture in dendrites from several epithermal deposits and concluded it is typical for native gold deposited from colloids in epithermal environment. Burke et al. (2017) observed gold nanoparticles via transmitted electron microscope in dendrites from the Round Mountain deposit. This suggests dendrites formed from gold nanoparticles are common in nature and colloidal transport of gold is possible.

However, dendrites from the Ametistovoe deposit show no evidence of mosaic texture and are chemically homogeneous. Band contrast maps show high crystallization degree and no grain

boundaries inside electrum grains (Fig. 6g), IPF maps show only rare twinning and sometimes insignificant misorientation (Fig. 6h); this evidences the dendrites are single crystalline. Electrum in quartz, in contrast, often has mosaic texture (Fig. 5e), comprising of chaotically oriented crystals of lower quality. Homogeneous composition of electrum observed on a sample-scale and grain-scale (dendrite-scale) for the Ametistovoe deposit implies all electrum in the studied sample, confined to both quartz and sphalerite, was precipitated under the same PTx conditions. This suggests either rapid crystallization of all electrum in the sample or its growth in environment isolated from any external factors. It appears that the PTX conditions were the same for both electrum within sphalerite and within quartz. This indicates gold and silver at the Ametistovoe deposit are likely to be transported in solution rather than as colloids which were nucleated in different parts of a vein under different PTx conditions.

Sphalerite

Sphalerite, along with galena, forms relatively large crystals and, unlike electrum, exhibits certain variability in chemical composition (FeS 5.8 to 8.8 mol.%) which can be interpreted as growth zoning. Such variability can be reflected by changes of S fugacity and/or temperature (Scott, 1983). These parameters would reflect also composition of electrum if it co-precipitated with sphalerite. This suggests sphalerite and galena deposited later than electrum and overgrew it. Chaotic orientation of sphalerite and galena crystals in relation to electrum dendrites (Figs. 5c,d) confirms this suggestion. The presence of primary fluid inclusions of low-salinity is further evidence for a hydrothermal origin of sphalerite. Depositional temperature was ca. 245 – 270^{o}C.

Quartz

Quartz globules with radial or jigsaw texture similar to those observed in the present study (Figs. 5f and 6b-e) are common in low sulfidation epithermal deposits worldwide (Dong et al., 1995; Taksavasu et al., 2018; Zeeck et al., 2021 and references therein), siliceous sinters of hot springs (Jones, 2021 and references therein), in geothermal power plants (Van den Heuvel et al., 2018) and were even found in mesothermal ores (Herrington and Wilkinson, 1993). Such globules are usually interpreted as recrystallization of amorphous silica. Dong et al. (1995) traced a chain of solidification and crystallization events from amorphous silica gel via flamboyant radial spheres to “ghost spheres” up to 300 microns in size. (Zeeck et al., 2021) studying epithermal ores in Omu camp (Japan) noted non-crystalline silica which co-precipitated with gold and silver minerals. This

observation is in agreement with experimental data of McNab et al. (2024) who conducted hydrothermal experimental simulation of coprecipitation of amorphous silica and gold nanoparticles and traced their subsequent recrystallization from amorphous silica via microspherules tens of microns in size to coarse crystalline quartz accompanied by relocation gold particles to quartz grain boundaries.

Radial flamboyant extinction is sometimes documented in epithermal ores (Dong et al., 1995) but radial twinning has not been revealed, perhaps because EBSD studies have been seldom applied to epithermal quartz textures. However, in agates Götze et al. (2019) reported microspherules composed of quartz micro-crystals radially oriented, established by IPF maps and proposed these were formed around a nucleus within amorphous silica gel via spiral growth. Such model explains the formation of twins with jugged boundaries.

Later idiomorphic quartz-2 overgrowing sphalerite and quartz-3 coexisting with chlorite could precipitate from solution which is evidenced by primary fluid inclusions at temperatures of ca. 220 – 260^{o}C.

Model of electrum dendrites formation

Models proposed to explain the formation of electrum dendrites in epithermal environment have been recently reviewed by Tharalson et al. (2023). Colloidal transport of silica forming colloform bands is not argued; for gold dendrites and their relations to silica, however, opinions are ambiguous. Saunders (1990) proposed that electrum dendrites grew from colloids (gold nanoparticles) which were nucleated in deeper part of the hydrothermal system and transported by the accenting fluid to the deposition site. This model, however, cannot be applied to the Ametistovoe deposit for the reasons discussed above.

One could also suggest the decomposition of early sphalerite with high contents of Au and Ag to sphalerite intergrown with electrum dendrites. However maximum solubility of Au (ca. 1 wt.%) was described in high-In sphalerite which was synthesized at 800^{o}C (Tonkacheev et al., 2019; Filimonova et al., 2019). Such a high temperature is unreal for epithermal environment bit if it was not 1 wt.% of Au would not be enough to form electrum particles which occupy several percent of sphalerite grain (Figs.5d, 6, 7a). In natural sphalerite Au content does not exceed several ppm (Cook et al., 2009; Tauson and Lipko, 2020 and references therein). Thus the decomposition of a gold-bearing sphalerite is not an appropriate mechanism for the formation of the observed patterns.

Numerous experiments of synthesis of single crystalline gold dendrites proved that the presence of various polymers is crucial in the formation of dendritic gold. Without polymers only agglomerate gold nanoparticles were obtained (Han et al., 2011; Lin et al., 2011; Huang et al., 2012 and references therein). The observed formation mechanism includes formation of gold nanoparticles which served as growth centers of the dendrites (Han et al., 2011; Huang et al., 2012). The role of polymers is to stabilize gold nanoparticles and to prevent their fast dissolution (Huang et al., 2012). Another important feature of polymers is their selective absorption on gold crystal faces. For example cysteine ($HO_2CCH(NH_2)CH_2SH$) molecules are selectively adsorbed on (100), (110) and other crystal faces but not on the (111) face. This blocks the growth of all faces except of (111) and results in formation of single-crystalline dendrites (Lin et al., 2011).

A similar scenario might be proposed for natural electrum crystalline dendrites. Silica gel, being polymerized, also can be selectively adsorbed by different crystal faces and triggers dendrites growth in one direction. Recently Monecke et al. (2023) suggested that electrum dendrites can grow within a previously formed gel-like silica bands. Such gel-like silica could deposit earlier but, being permeable, allows the diffusion of dissolved Au through the gel from the fluid flowing across the silica layer. This model implies Au is transported in solution (Monecke et al., 2023; Tharalson et al., 2023), however the formation of gold nanoparticles and the existence of colloidal gold cannot be ruled out at some stages. Dendrites covered by a silica gel can develop single crystals and, moreover silica gel may maintain more or less stable PTx conditions to form crystals with relatively constant chemical composition. This statement, however, is equivocal because some experimental works reported stirring as a critical factor for growth of single crystalline dendrites (Han et al., 2011) while the others obtained similar dendrites without stirring (Bauer et al., 2020). Another important role of a silica gel is that it protects growing dendrites from dissolution or mechanical damage.

In case of the Ametistovoe deposit, electrum dendrites might grow within silica gel (Fig. 8a) either contemporaneously with or immediately after the deposition of silica gel. Subsequently silica gel could be either partly removed by new flows of a fluid or partly solidified and, thus, reduced in volume and left dendrites partly in the open space. Later dendrites left in the open space were overgrown by sphalerite-1 and minor chalcopyrite-1, galena-1 (Fig. 8b). At least, most elements at this stage were transported in solution which is evidenced by fluid inclusions in dendrite-bearing sphalerite. Depositional temperature was ca. 245 – 270°C. At the same time, or, perhaps, slightly later, opaline silica recrystallized to microcrystalline globular quartz which resulted in destruction of

electrum dendrites located within silica (Fig. 8c). This explains mosaic texture observed in electrum from quartz; at the same time chemical composition of electrum remained untouched. Deposition of sphalerite-1 was followed by the formation of druse-like quartz, followed by pyrite, sphalerite-2, galena-2, and chalcopyrite-2. (Fig. 8c). Idiomorphic quartz-2 crystals and chlorite postdated sulfides deposition (Fig. 8d) at temperatures of about 220 – 260^{o}C. This model explains the absence of electrum dendrites within quartz and the presence of irregularly shaped electrum with the same composition and low pattern quality within quartz. Electrum dendrites overgrown by sphalerite and other sulfides “survived” and preserved their morphology and single crystal features.

Conclusions

In contrast to most natural dendrites which are composed of nanoparticles, electrum dendrites from ores of the Ametistovoe Au-Ag epithermal deposit are proved to be single crystalline. They are chemically homogeneous with a fineness of ca. 600-620.

The dendrites in most cases are 2-dimensional, rarely 3-dimensional, and consist of one trunk and branches which overgrow it on (100), sometimes (111) plane.

Electron back-scattered diffraction has proven as a powerful tool for study gold dendrites and to decipher silica recrystallization textures.

A model proposed for dendrites formation assumes they grew from solution within a silica gel and then were partly overgrown by sphalerite. Dendrites within sphalerite were not subjected to later maturation while those within silica were completely destructed due to crystallization of silica gel.

Silica gel is a key precursor for formation of single crystal gold dendrites which is in an agreement with experimental data.

Funding

The research was carried out within the framework of a state order to the Institute of Geology of Ore Deposits, Petrography, Mineralogy and Geochemistry, Russian Academy of Sciences. X-ray computed microtomography was performed within the framework of project 125021702335-5. EMPA analysis was sponsored by the Natural History Museum (NHM London) via the CERCAMS Fellowship Program hosting study visit of OP in 2010.

Acknowledgements

The authors thank V.A. Kovalenker and I.A. Morozov (IGEM RAS), I.O. Galuskina and E.V. Galuskin (University of Silesia) for useful discussion and assistance with data processing. M.S.

Lozhkin (St. Petersburg State University) is acknowledged for plasma etching of the samples; John Spratt (formerly NHM) is warmly thanked for EMPA analyses. Constructive comments and suggestions of the four reviewers are also highly appreciated.

Competing interests. The authors declare no competing interests

References

Bailey S.W. (1988) Chlorites: structures and crystal chemistry. Pp. 347–403 in: *Hydrous Phyllosilicates (Exclusive of Micas)* (S.W. Bailey editor). Reviews in Mineralogy, 19.

Barton P.B. and Toulmin P. (1964) The electrum – tarnish method for the determination of the fugacity of sulfur in laboratory sulfide systems. *Geochimica et Cosmochimica Acta*, **28,** 619–640.

Bauer P., Mougin K., Faye D., Buch A., Ponthiaux P. and Vignal V. (2020) Synthesis of 3D dendritic gold nanostructures assisted by a templated growth process: application to the detection of traces of molecules. *Langmuir*, **36(37)**, 11015–11027. doi: 10.1021/acs.langmuir.0c01857

Betekhtin A.G., Genkin A.D., Filimonova A.A. and Shadlun T.N. (1958) *Ore textures and structures*. Gosgeoltekhizdat, Moscow, 444 pp. [in Russian].

Bodnar R.J. and Vityk M.O. (1994) Interpretation of microthermometric data for H_2O–NaCl fluid inclusions. Pp. 117–130 in: *Fluid Inclusions in Minerals, Methods and Applications* (B. De Vivo and M.L. Frezzotti editors), Virginia Tech, Blacksburg, VA.

Borisova E.A. (2010) Native gold from Mutnovskoe ore occurrence, South-Eastern Kamchatka, Russia. New Data on Minerals, **45**, 66–71.

Bortnikov N.S. and Tolstykh N.D. (2023) Epithermal Deposits of Kamchatka, Russia. *Geology of Ore Deposits,* **65** (Suppl 1), S124–S152. https://doi.org/10.1134/S1075701523070176

Boydell H.C. (1925) The role of colloidal solutions in the formation of mineral deposit. *Institutions of Mining and Metallurgy Transactions*, **34**, 145–337.

Brodusch N., Demers H., and Gauvin, R. (2018). Imaging with a commercial electron backscatter diffraction (EBSD) camera in a scanning electron microscope: A review. *Journal of Imaging*, **4**(7), 88.

Burke M., Rakovan J. and Krekeler M. P. (2017) A study by electron microscopy of gold and associated minerals from Round Mountain, Nevada. *Ore Geology Reviews*, **91**, 708–717.

Butt C.R., Hough R.M. and Verrall M. (2020) Gold nuggets: the inside story. *Ore and Energy Resource Geology*, **4**, 100009.

Cathelineau M. (1988) Cation Site Occupancy in Chlorite and Illites as a Function of Temperature. *Clay Minerals*, **23**, 471–485.

Chapman R.J., Banks D.A., Styles M.T., Walshaw R.D., Piazolo S., Morgan D.J., Grimshaw M.R., Spence-Jones C.P., Matthews T.J. and Borovinskaya O. (2021) Chemical and physical heterogeneity within native gold: implications for the design of gold particle studies. *Mineralium Deposita,* **56**, 1563–1588. doi: 10.1007/s00126-020-01036-x

Chen H., Wang Y. and Dong S. (2007). An effective hydrothermal route for the synthesis of multiple PDDA-protected noble-metal nanostructures. *Inorganic chemistry*, **46**, 10587-10593.

Chukhrov F.V., 1955. *Colloids in the Earth's Crust*. Izd. Akad. Nauk SSSR, Moscow. 672 pp. [in Russian]

Cook N.J., Ciobanu C.L., Pring A., Skinner W., Shimizu M., Danyushevsky L., Saini-Eidukat B., Melcher F. (2009). Trace and minor elements in sphalerite: A LA-ICPMS study. *Geochimica et Cosmochimica Acta*, **73**, 4761–4791.

Crawford M.L. (1981) Phase equilibria in aqueous fluid inclusions. Pp. 75–100 in: *Fluid Inclusions: Applications to Petrology* (L.S. Hollister and M.L. Crawford editors), **6**. Mineralogical Association of Canada Short Course Handbook.

Dong G., Morrison G. and Jaireth, S. (1995). Quartz textures in epithermal veins, Queensland; classification, origin and implication. *Economic geology*, **90**, 1841-1856.

Filimonova O.N., Trigub A.L., Tonkacheev D.E., Nickolsky M.S., Kvashnina K.O., Chareev D.A., Chaplygin I.V., Lafuerza S., Tagirov B. R. (2019). Substitution mechanisms in In-, Au-, and Cu-bearing sphalerites studied by X-ray absorption spectroscopy of synthetic compounds and natural minerals. *Mineralogical Magazine*, **83**, 435–451.

Frondel C. (1938) Solubility of colloidal gold under hydrothermal conditions. *Economic Geology*, **33**, 1–20.

Götze J., Berek H. and Schäfer K. (2019) Micro-structural phenomena in agate/chalcedony: Spiral growth. *Mineralogical Magazine*, **83**, 281–291.

Granovsky A.G. (1993) The Ametistovoe gold-silver deposit (Kamchatka) – thermobarogeochemistry and exploration potential. *Ores and Metals,* (1 – 2), 87–97. [in Russian]

Grimshaw M., Chapman R.J. and Pearce M.A. (2017) Characterization of the crystallography of gold using EBSD. *Applied Earth Science*, **126**, 60–61.

Herrington R.J. and Wilkinson J.J. (1993) Colloidal gold and silica in mesothermal vein systems: Geology, 21, 6, 539–542. doi: 10.1130/0091-7613(1993)021<0539:CGASIM>2.3.CO;2

http://zolkam.ru/actives/8101 (last addressed 24/07/2024)

https://nedradv.ru/nedradv/ru/places (last addressed 25/03/2025)

Huang D., Qi Y., Bai X., Shi L., Jia H. Zhang, D. and Zheng L. (2012) One-pot synthesis of dendritic gold nanostructures in aqueous solutions of quaternary ammonium cationic surfactants: effects of the head group and hydrocarbon chain length. *ACS Applied Materials & Interfaces*, **4**, 4665–4671.

Jones B. (2021) Siliceous sinters in thermal spring systems: Review of their mineralogy, diagenesis, and fabrics. *Sedimentary Geology*, **413**, 105820.

Jhabvala J, Boillat E and Glardon R. (2011) On the use of EBSD analysis to investigate the microstructure of gold samples built by selective laser melting. *Gold Bulletin*, **44**, 113–118.

Kotelnikov A.R., Suk N.I., Kotelnikova Z.A., Tschekina T.I. and Kalinin G.M. (2012) Mineral geothermometers for low temperature paragenesis. *Vestnik Otdelenia nauk o Zemle*, **4**, NZ9001, doi:10.2205/2012NZ_ASEMPG.

Kozin A.K., Stepanov S.Y., Palamarchuk R.S., Shilovskikh V.V. and Zhdanova V.S. (2023) Mineral Associations of Concentrates from Gold-Bearing Placers of the Miass Placer Zone (South Urals) and Possible Primary Sources of Gold. *Russian Geology and Geophysics*, **64**, 1015–1030.

Kranidiotis P. and McLean W.H. (1987) Systematics of Chlorite Alteration at the Phelps Dodge Massive Sulfide Deposits, Matagami Quebec. *Economic Geology*, **82**, 1898–1911.

Li C., Shuford K.L., Chen M., Lee E.J. and Cho S.O. (2008) A facile polyol route to uniform gold octahedra with tailorable size and their optical properties. *ACS nano*, **2**, 1760–1769.

Liang Y., and Hoshino K. (2015) Thermodynamic calculations of Au_xAg_{1-x}–Fluid equilibria and their applications for ore-forming conditions. *Applied Geochemistry*, **52**, 109–117.

Lin T.H., Lin C.W., Liu H.H., Sheu J.T. and Hung W.H. (2011) Potential-controlled electrodeposition of gold dendrites in the presence of cysteine. *Chemical communications*, **47**, 2044–2046.

Lindgren W. (1915) Geology and mineral deposits of the National Mining district, Nevada. U.S. *Geological Survey Bulletin*, **601**, 58 pp.

Litvinov A.F., Patoka M.G., Markovsky B.F., Frolov Y.F., Koliada A.A., Pozdee A.I., Pavlova L.E. (1999) *Mineral resources map of the Kamchatka oblast, scale 1:500 000. Brief explanatory note*. VSEGEI publisher, Petropavlovsk-Kamchatsky, 563 pp. [in Russian].

Liu H. and Beaudoin G. (2021) Geochemical signatures in native gold derived from Au-bearing ore deposits. *Ore Geology Reviews*, **132**, 104066.

Maitland T. and Sitzman S. (2007) EBSD technique and materials characterization. Pp. 41–76 in: *Scanning microscopy for nanotechnology: Techniques and applications* (Zhou, W. and Wang, Z.L. editors). Springer, New York.

McNab R.R., Brugger J., Voisey C.R. and Tomkins A.G. (2024) Coprecipitation of amorphous silica and gold nanoparticles contributes to gold hyperenrichment. *Geology*, **52**, 737–741. doi: 10.1130/G52138.1

Morrison G.W., Rose W.J. and Jaireth S. (1991) Geological and geochemical controls on the silver content (fineness) of gold in gold–silver deposits. *Ore Geology Reviews*, **6**, 333–364.

Monecke T., Reynolds T.J., Taksavasu T., Tharalson E.R., Zeeck L.R., Guzman M., Gissler G. and Sherlock R. (2023) Natural growth of gold dendrites within silica gels. *Geology*, **51**, 189–192.

Nekrasov I.Ya. (1996) Volcano-cupola structure of the Ametist Deposit and zonality of gold-silver mineralization. *Doklady Earth Sciences*, **347A**, 382–384.

Northover S. M. and Northover J. P. (2012) Applications of Electron Backscatter Diffraction (EBSD) in Archaeology, Pp 76–85. In: *Historical Technology, Materials and Conservation: SEM and Microanalysis.* (Meeks N., Cartwright C., Meek A. and Mongiatti A. editors). Archetype Publications, London.

Novgorodova M.I. (2005) Metacolloidal gold. *New Data on Minerals*. **40**, 106–114.

Palyanova G., Kutyrev A., Beliaeva T., Shilovskikh V., Zhegunov P., Zhitova E. and Seryotkin Y. (2023) Pd,Hg-Rich Gold and Compounds of the Au-Pd-Hg System at the Itchayvayam Mafic-Ultramafic Complex (Kamchatka, Russia) and Other Localities. *Minerals*, **13**, 549. doi: 10.3390/min13040549

Petrenko I.D. (1999) *Gold-silver formations of Kamchatka*. Petropavlovsk-Kamchatskii: St-Peterburg Cartographic Factory VSEGEI. 115 pp. [in Russian].

Petrovskaya N.V. (1973) *Native Gold*. Nauka, Moscow, 345 pp. [in Russian].

Petrovskaya N.V., Novgorodova M.I., Frolova K.E. and Tsepin A.I. (1977) Nature of Heterogeneity and Phase Composition of Endogenic Native Gold. Pp. 75–88. In: *Neodnorodnost'*

mineralov i tonkie mineral'nye smesi (Heterogeneity of Minerals and Fine Mineral Mixtures). Nauka, Moscow, [in Russian].

Potter II R.W. (1977) Pressure corrections for fluid-inclusion homogenization temperatures based on the volumetric properties of the system NaCl-H_2O. *Journal of Research of the U.S. Geological Survey*, **5**, 603–607.

Prior D.J., Boyle A.P. Brenker F. Cheadle M.C., Day A., Lopez G., PERUZZO L., Potts G.J., Reddy S., Spiess R., Timms N.E., Trimby P., Wheeler J. and Zetterstrom L. (1999) The application of electron backscatter diffraction and orientation contrast imaging in the SEM to textural problems in rocks. *American Mineralogist*, **84**, 1741–1759.

Ramdohr P. (1969) *The Ore Minerals and their Intergrowths*. Pergamon Press, Oxford. 1174 pp.

Saunders J.A. (1990) Colloidal transport of gold and silica in epithermal precious metal systems: evidence from the Sleeper deposit, Humboldt County, Nevada. *Geology*, **18**, 757–760

Saunders J.A. and Burke M. (2017) Formation and aggregation of gold (electrum) nanoparticles in epithermal ores. *Minerals*, **7**, 163.

Saunders J.A. and Schoenly P.A. (1995) Fractal structure of electrum dendrites in bonanza epithermal Au-Ag deposits. Pp. 251–261. In: *Fractals in the earth sciences*. Springer US, Boston, MA.

Saunders J. A., Burke M. and Brueseke M.E. (2020) Scanning-electron-microscope imaging of gold (electrum) nanoparticles in middle Miocene bonanza epithermal ores from northern Nevada, USA. *Mineralium Deposita*, **55**, 389–398.

Roedder E. (1984) Fluid inclusions. *Reviews in Mineralogy*, **12**.

Schwartz A.J., Kumar M., Adams B.L. and Field D.P. (2009) *Electron backscatter diffraction in materials science*. Springer, New York, 393 pp.

Scott S.D. (1983) Chemical Behavior of Sphalerite and Arsenopyrite in Hydrothermal and Metamorphic Environments. *Mineralogical Magazine*, **47**, 427–435.

Sillitoe R.H. and Hedenquist J.W. (2003) Linkages between volcanotectonic settings, ore-fluid compositions, and epithermal precious metal deposits. *Society of Economic Geologists Special Publication*, **10**, 315–343.

Simmons S.F., White N.C. and John D.A. (2005) Geological characteristics of epithermal precious and base metal deposits. *Economic Geology 100th Anniversary Volume*, **100**, 485–522.

Shikazono N. (1985) A comparison of temperatures estimated from the electrum–sphalerite–pyrite–argentite assemblage and filling temperatures of fluid implications from epithermal Au-Ag vein-type deposits in Japan. *Economic Geology*, **80**, 1415–1424.

Taksavasu T., Monecke T. and Reynolds T.J. (2018) Textural characteristics of non-crystalline silica in sinters and quartz veins: implications for the formation of bonanza veins in low-sulfidation epithermal deposits. *Minerals,* **8**, 331.

Tauson V.L. and Lipko S.V. (2020) Solubility of gold in common gold-concentrating minerals. *Russian Geology and Geophysics*, **61**, 1331–1344.

Tonkacheev D.E., Chareev D.A., Abramova V.D., Kovalchuk E.V., Vikentyev I.V. and Tagirov B.R. (2019) The substitution mechanism of Au in In-, Fe- and In-Fe-bearing synthetic crystals of sphalerite, based on the data from EPMA and LA-ICP-MS study. *Litosfera*, **19**, 148–161. doi: 10.24930/1681-9004-2019-19-1-148-161

Tharalson E.R., Taksavasu T., Monecke T., Reynolds T.J., Kelly N.M., Pfaff K., Bell A.S. and Sherlock R. (2023) Textural characteristics of ore mineral dendrites in banded quartz veins from low-sulfidation epithermal deposits: implications for the formation of bonanza-type precious metal enrichment. *Mineralium Deposita*, **58**, 1395–1419.

Van den Heuvel D.B., Gunnlaugsson E., Gunnarsson I., Stawski T.M., Peacock C.L. and Benning L.G. (2018) Understanding amorphous silica scaling under well-constrained conditions inside geothermal pipelines. *Geothermics*, **76**, 231–241.

Vartanyan S.S., Oreshin V.Y. and Khvorostov V.P. (1988) The Ametistovoe deposit. Pp. 244–250. In: *Gold deposits of the USSR. V.4. Geology of gold deposits of the East of the USSR* (Narseev V.A., Timofeevsky D.A. and Yanovsky V.M. editors). TSNIGRI publisher, Moscow. (in Russian).

Yuan Y.J., Andrews M.K. and Marlow B.K. (2004) Chaining and dendrite formation of gold particles. *Applied Physics Letters*, **85**, 130–132.

Zeeck L.R., Monecke T., Reynolds T.J., Tharalson E.R., Pfaff K., Kelly N.M. and Hennigh Q.T. (2021) Textural characteristics of barren and mineralized colloform quartz bands at the low-sulfidation epithermal deposits of the Omu camp in Hokkaido, Japan: Implications for processes resulting in bonanza-grade precious metal enrichment. *Economic geology*, **116**, 407–425.

Figure captions

Figure 1. Schematic geological map of the Ametistovoe ore field (Vartaian et al., 1988; North Kamchatka survey data) and the cross-section; the inset shows the position of the deposit marked by a diamond symbol, modified after (Litvinov et al., 1999).

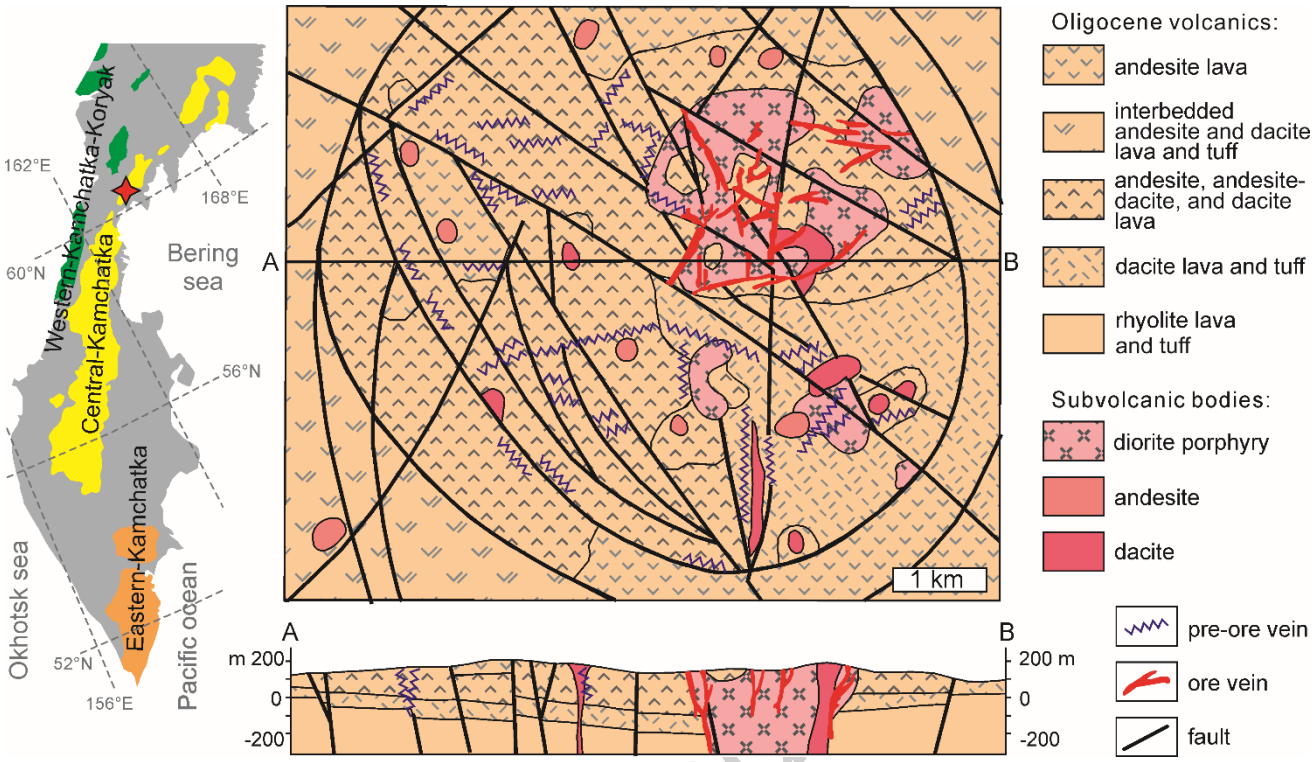

Figure 2. Images of typical ore textures of the studied samples.

a – Photograph of a polished section of a zoned quartz-sulfide veinlet. Box shows the location of Fig. 2b; b – Photograph of a portion of Fig 2a using a stereomicroscope, showing mineral sequence within the veinlet; c– Photomicrograph (reflected light) showing sphalerite-1 with galena, both with oval inclusions of electrum and also irregularly shaped electrum in (mosaic) quartz-1; d,e) Paired photomicrographs of a doubly-polished section showing electrum dendrites and inclusions within sphalerite-1 in reflected light (d) and transmitted light (e); f,g) Paired photomicrographs similar to d,e showing electrum dendrites and inclusions within sphalerite-1 and locally galena-1 (reflected light, f, and transmitted light, g); h) Photomicrograph (reflected light) showing electrum-free sphalerite-2 and galena-2 overgrown by quartz-2 and crosscut by a later quartz-2 veinlet.

ABBREVIATIONS: Qtz– quartz, Chl– chlorite, Sp– sphalerite, Gn– galena, Ccp– chalcopyrite, Au– electrum; 1, 2, 3 indicate distinct generations of a mineral.

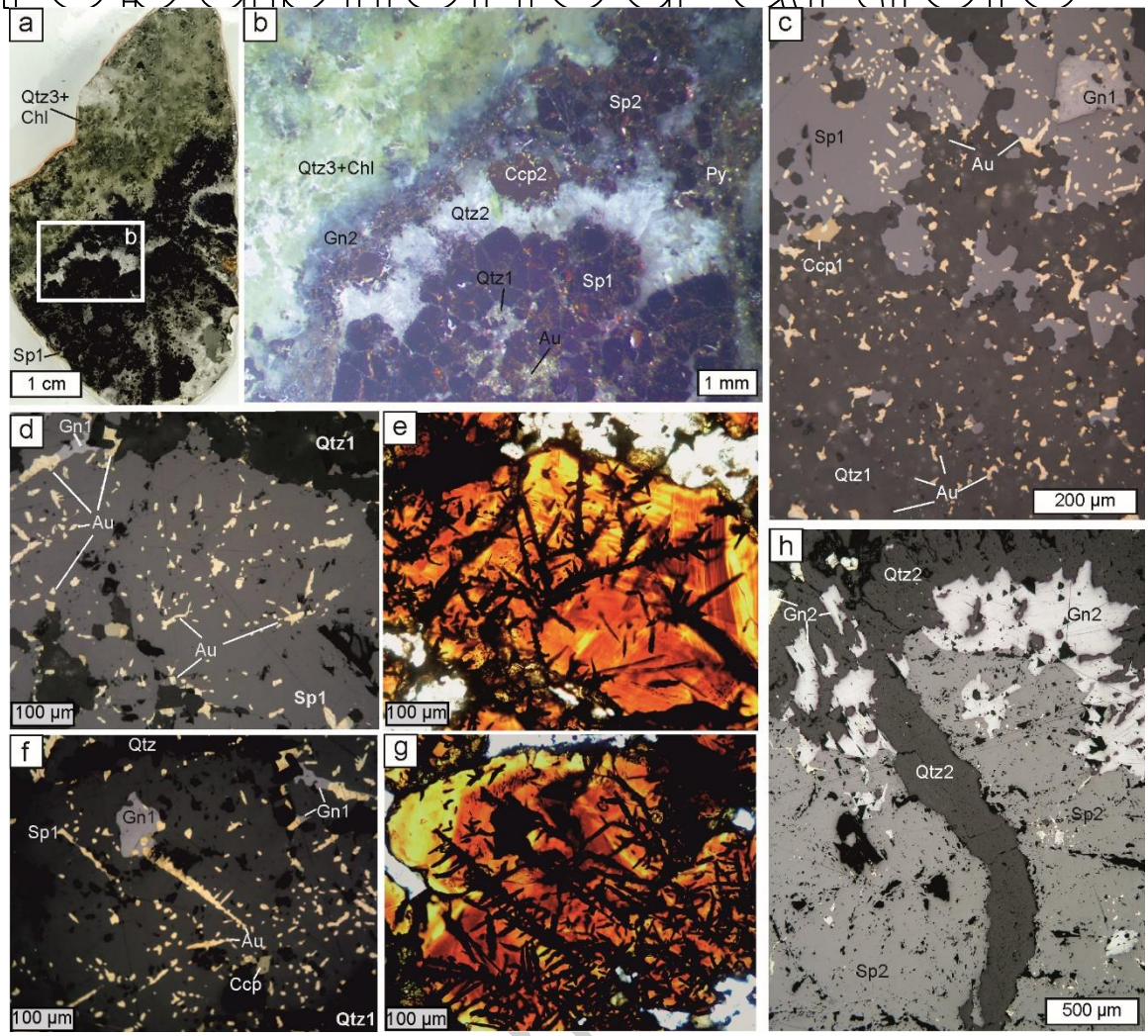

Figure 3. Fluid inclusions in sphalerite-1 (a) and quartz-2 (b), transmitted light; c– homogenization temperature vs. salinity diagram for fluid inclusions in quartz and sphalerite.

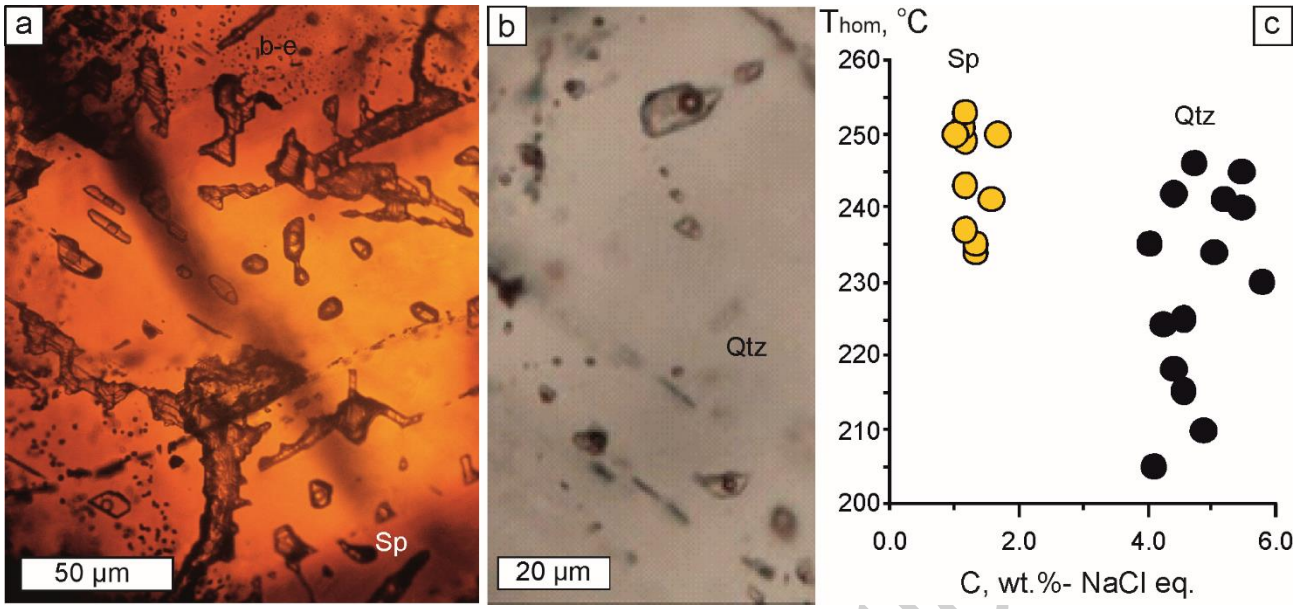

Figure 4. X-ray computed tomography 3-dimensional images of 2 mm cylinders where the different grey levels represent the different minerals. General view (a) and fragments where quartz and sphalerite were reduced to liberate electrum dendrites (b to e). b– several dendrites; c– dendrites with angles between “trunk” and “branches” closed to 90° and 60°; d and e– 3-dimensional “bush”, aside (d) and top (e) views.

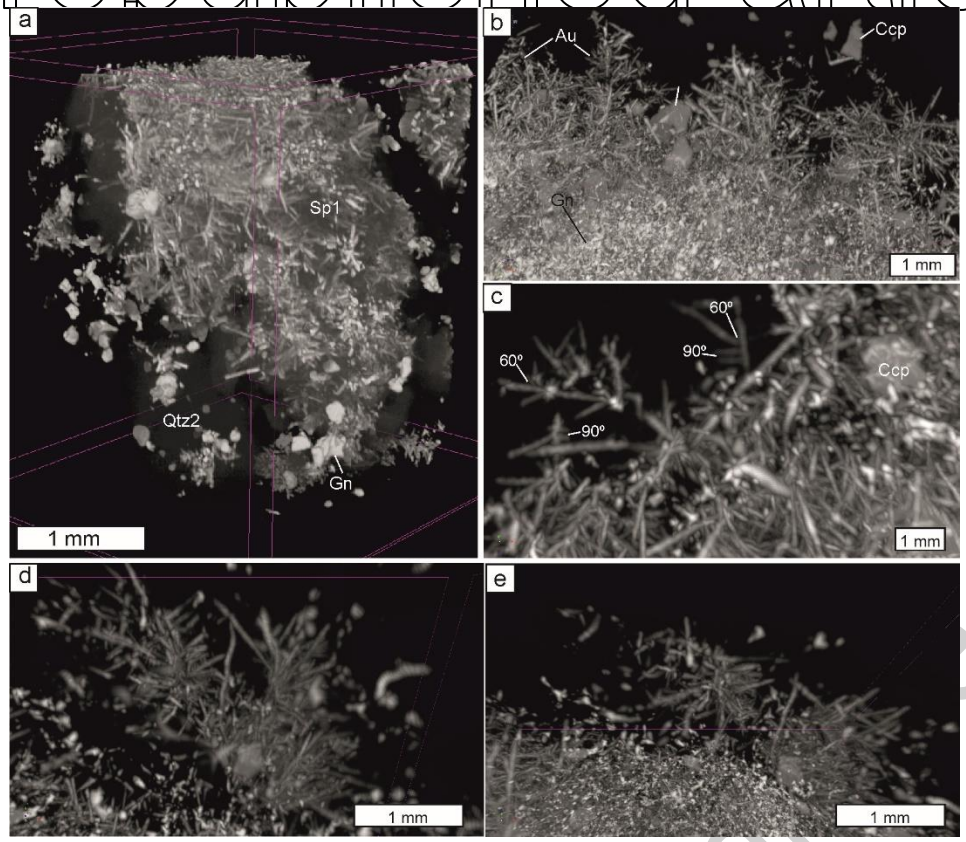

Figure 5. Back-scattered electron (SEI) and EBSD images for electrum intergrown with quartz-1 and sulfides.

a-d – relationships between electrum, quartz-1, and sphalerite-1 in the same site (box shows the position of figs. e and f): a – back-scattered electron image showing oval electrum within sphalerite-1 and irregularly shaped electrum within quartz-1; b – band contrast map (step 2 μm) showing lighter color (i.e. higher crystallinity degree) for electrum within sphalerite-1 compared to electrum within quartz-1; c – IPF(z) orientation maps for sphalerite-1 only, overlapped onto band contrast map, showing twinning in large anhedral sphalerite crystals; d – IPF(x) orientation map for electrum only, overlapped onto band contrast map, note each cluster with a unique color corresponds to a separate dendrite within sphalerite; e and f – detail of (b), e– random orientation of electrum and mosaic texture of quartz and electrum within it; f– IPF(x) figure of quartz with mosaic texture and radial twinning, highlighted by dotted lines.

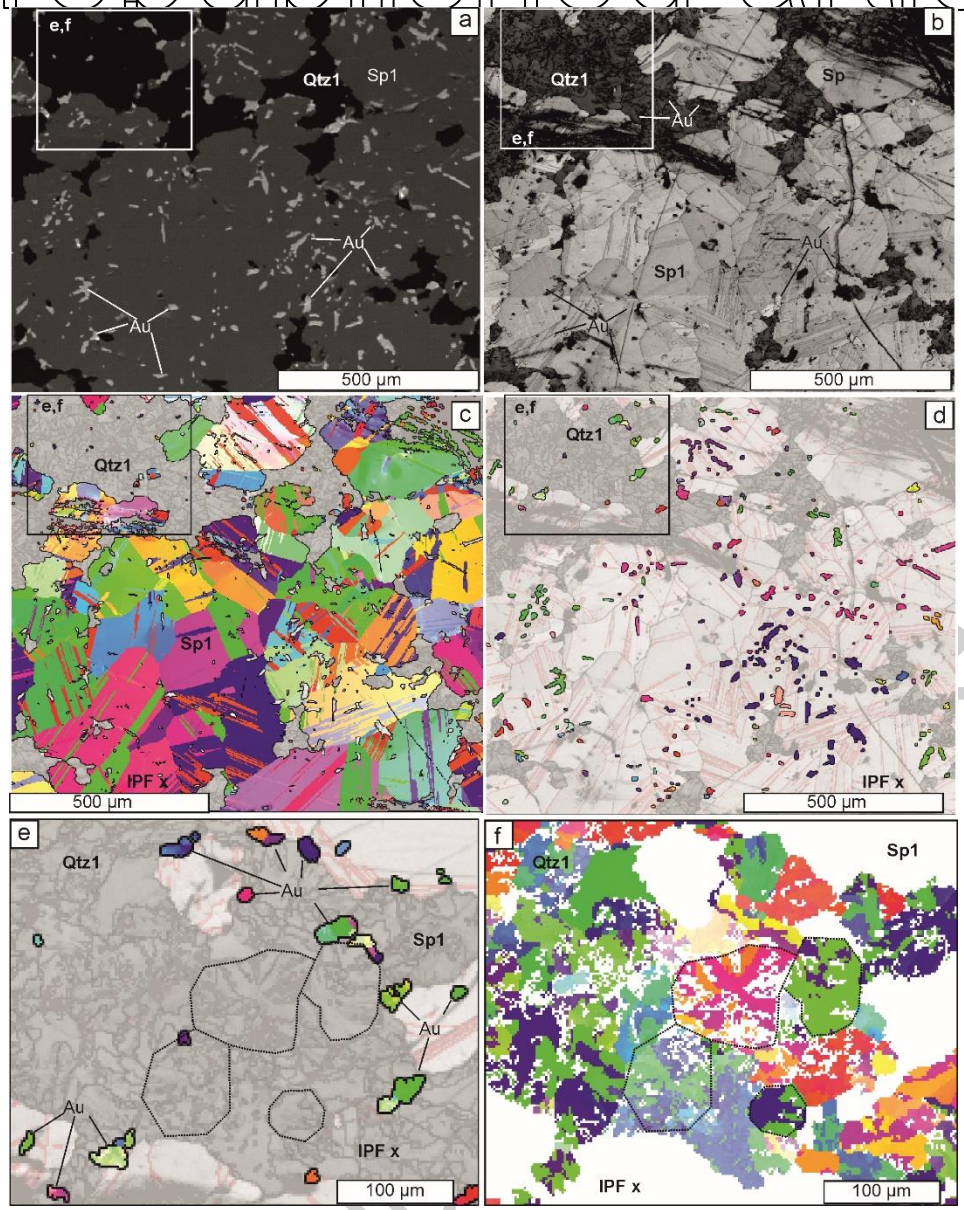

Figure 6. EBSD images for quartz intergrown with sulfides and electrum.

a – back-scattered electron image of electrum, sphalerite-1, and galena-1 within quartz-1; b – IPFx orientation map for quartz (step 2 µm) of the same site, note spherical quartz-1 grains with radial twinning, highlighted by dotted lines, and jugged twin boundaries marked by arrows, boxes show locations of Figs c, d, and e; c and d – band contrast images of (b) showing radial texture of quartz-1 grains; e – fragment of (b), IPFx orientation map for electrum and quartz (step 1 µm); f– misorientation profile along the board between “trunk” and “branch” (marked by an arrow on (e); g and h – band contrast and IPFy orientation maps respectively for electrum and sphalerite (step 0.1 µm), minor misorientation of electrum is marked by arrows.

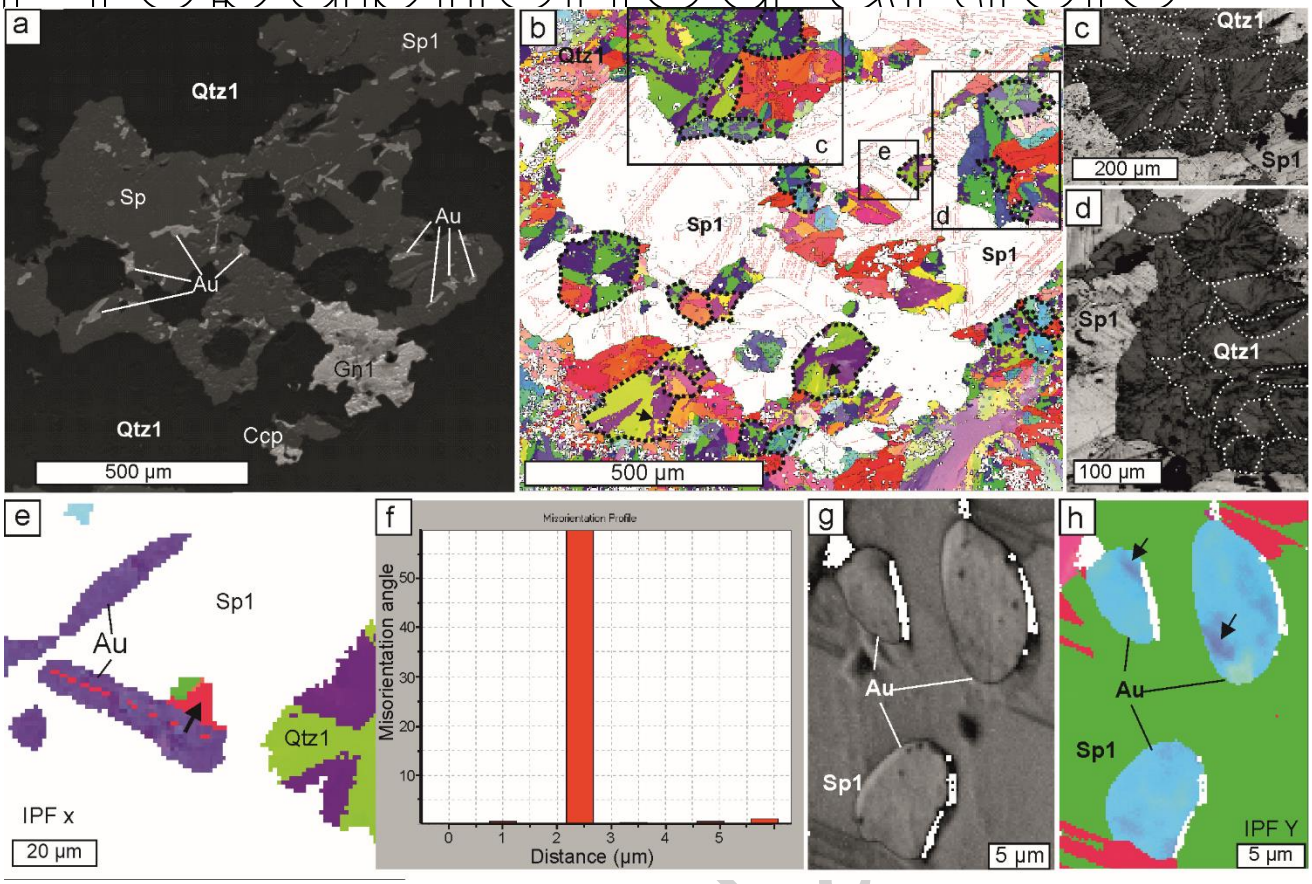

Figure 7. Relationships of electrum, sphalerite-1, galena-1, and quartz-1, step 1 µm: a – phase map; b – IPF(y) orientation map (step 1 µm) for electrum within sphalerite and galena, note that the same dendrite (yellow color) is intergrown with sphalerite-1 and galena-1; c and d– $Ag_{L\alpha}$ and $Au_{L\alpha}$ X-ray maps, note chemical composition of electrum does not vary either within the same cluster or from one cluster to another.

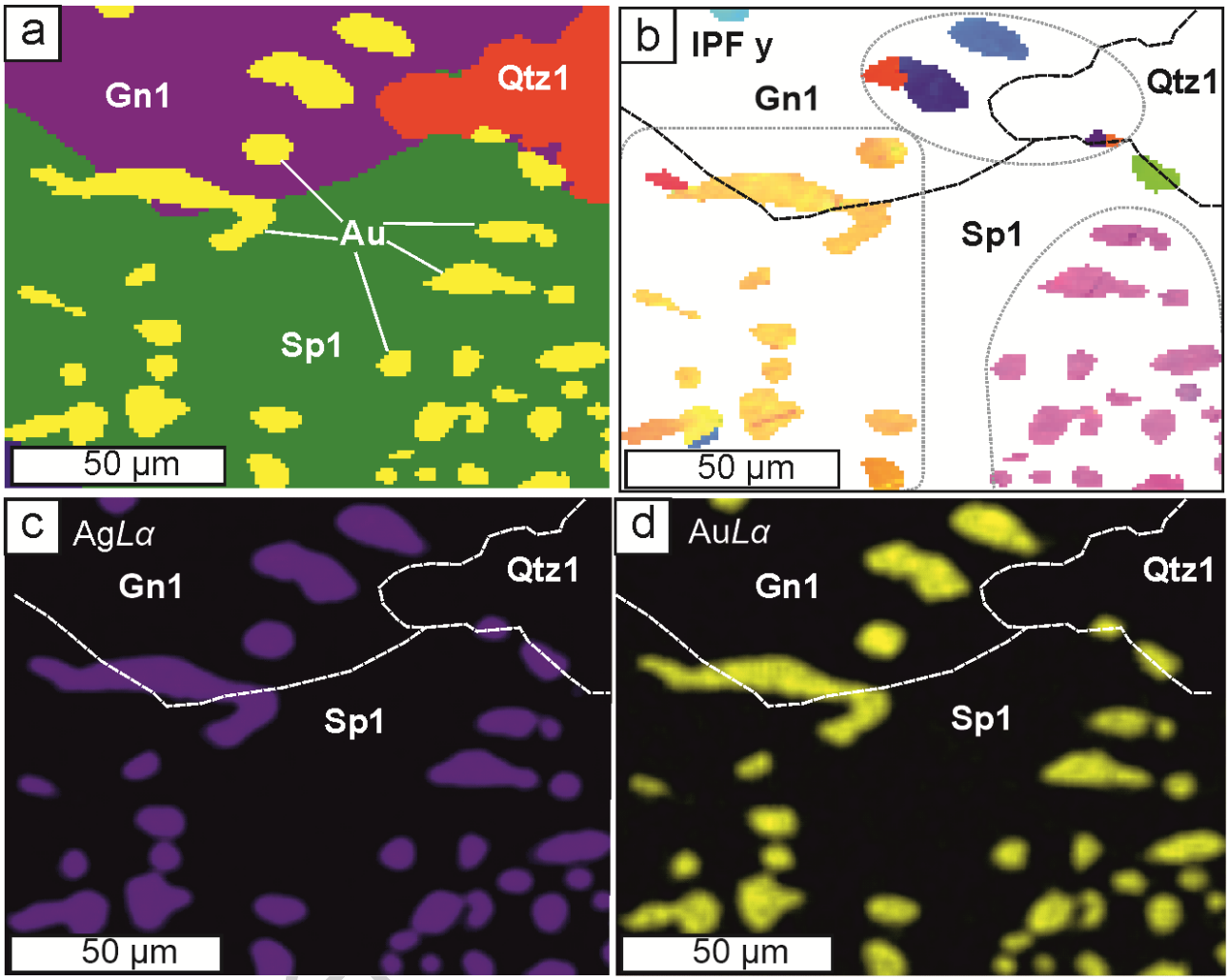

Figure 8. Proposed model for electrum dendrite growth and maturation in the Ametistovoe deposit. Modified from Monecke et al. (2023) and Tharalson et al. (2023).

a– electrum dendrites grow contemporaneously with or immediately after the deposition of the silica host along the vein wall, silica is transported in colloids while Au and Ag can be transported in solution, dendrites grow both within silica gel and in open space; b– dendrites are overgrown by sphalerite-1 and minor galena, pyrite and chalcopyrite-1, and, later by sphalerite-2; c– crystallization of silica results in destruction of electrum dendrites, this process might have started immediately after silica deposition and last during deposition of sulfides, formation of crystalline

quartz followed by pyrite, sphalerite 2, chalcopyrite 2, galena-2 which overgrow quartz and sphalerite-1 and fill cracks in sphalerite; d– deposition of quartz crystals and chlorite.

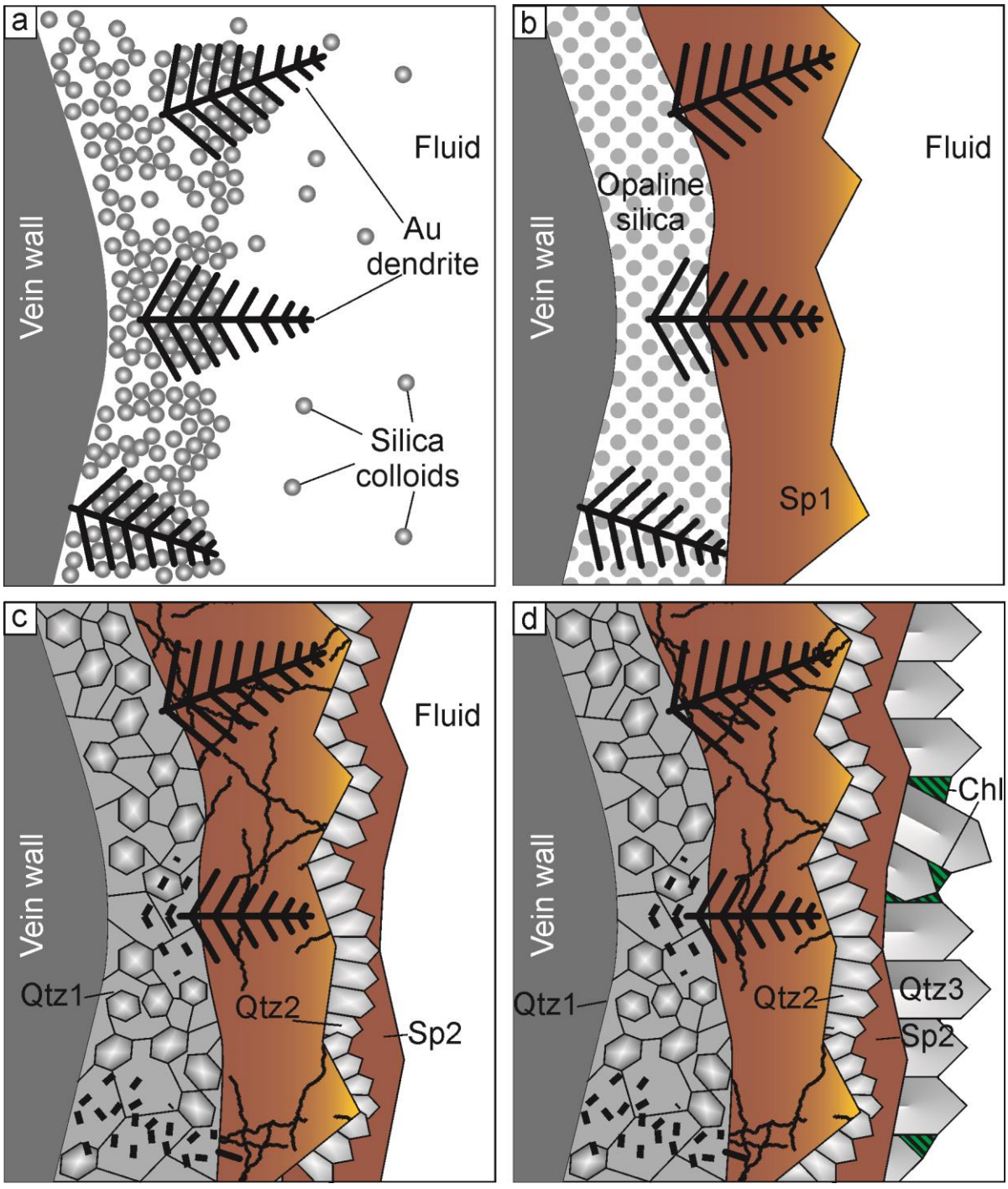

Supplementary material. The supplementary material for this article can be found at .....

ESM 1. EMPA points locations

ESM 2. X-ray tomography

ESM 3. EBSD data

Table 1. Selected chemical composition of electrum (Wt.%)

No	Host mineral	Ag	Au	Hg	Total	Fineness
1.	Sphalerite	39.36	61.43	0.28	101.07	608
2.	– " –	39.13	62.08	0.28	101.49	612
3.	– " –	39.72	61.34	0.34	101.40	605
4.	– " –	39.32	61.03	0.46	100.81	605
5.	– " –	39.53	61.49	0.33	101.35	607
6.	– " –	39.67	61.02	0.28	100.97	604
7.	– " –	39.78	60.88	0.36	101.02	603
8.	Quartz	39.38	62.14	0.27	101.79	610
9.	– " –	38.94	62.58	0.30	101.82	615
10.	– " –	39.15	61.66	0.25	101.06	610

Table 2. Selected chemical composition of sphalerite (Wt.%)

No	S	Fe	Zn	Cu	Mn	Cd	Total	FeS, Mol.%
Sphalerite 1								
1.	33.04	3.68	63.01	0.05	0.12	0.26	100.16	6.38
2.	33.66	3.75	62.81	0.08	0.12	0.26	100.68	6.44
3.	33.69	3.54	62.79	<dl	0.12	0.26	100.40	6.10
4.	33.56	3.34	63.15	0.08	0.12	0.24	100.49	5.76
5.	33.51	3.47	62.97	0.07	0.13	0.25	100.40	5.98
6.	33.40	3.98	62.09	0.10	0.13	0.26	99.96	6.90
7.	34.09	3.60	63.05	<dl	0.11	0.25	101.10	6.14
8.	33.59	3.58	62.97	<dl	0.12	0.24	100.51	6.16
9.	33.61	3.64	62.19	0.13	0.13	0.26	99.96	6.28
10.	33.78	3.44	63.38	<dl	0.11	0.23	100.94	5.90
11.	33.79	3.54	63.22	<dl	0.11	0.25	100.91	6.06
12.	33.77	3.94	62.76	0.07	0.11	0.25	100.90	6.76
13.	33.73	5.14	60.82	0.08	0.14	0.23	100.14	8.84
Sphalerite 2								
14.	33.75	3.58	63.17	<dl	0.10	0.24	100.84	6.16
15.	33.66	3.50	63.27	<dl	0.10	0.22	100.75	6.02
16.	33.41	4.34	62.07	<dl	0.15	0.28	100.25	7.48
17.	33.74	4.93	61.41	0.10	0.18	0.27	100.63	8.46
18.	33.39	4.76	61.72	0.10	0.15	0.27	100.39	8.22
19.	33.14	4.23	61.73	0.06	0.14	0.24	99.54	7.36
20.	33.54	2.01	63.97	0.05	0.06	0.23	99.86	3.48

Table 3. Chemical composition of chlorite (Wt.%)

No	1	2	3	4	5	6	7	8	9	10
SiO_2	25.41	26.48	26.83	26.61	25.76	26.76	26.16	24.56	26.12	26.12
Al_2O_3	15.13	14.71	15.36	15.56	15.58	16.02	16.70	15.07	15.39	15.39
FeO	30.68	30.10	30.89	29.68	29.46	30.57	30.39	28.48	30.21	30.21
MnO	1.43	1.47	1.72	1.55	1.46	1.48	1.72	1.48	1.50	1.50
MgO	9.92	10.07	10.08	10.12	9.60	10.17	10.58	9.35	10.30	10.30
Total	82.58	82.84	84.87	83.52	81.86	85.00	85.54	78.95	83.52	83.52
X(Mg)	0.36	0.36	0.36	0.37	0.36	0.36	0.37	0.36	0.37	0.37
Al(IV)	2.01	1.78	1.85	1.82	1.89	1.89	2.08	1.96	1.93	1.93
Al(VI)	2.19	2.29	2.31	2.44	2.47	2.42	2.37	2.41	2.28	2.28
Si/Al	1.43	1.53	1.48	1.45	1.40	1.42	1.33	1.38	1.44	1.44
T1	262	225	235	231	242	242	273	253	249	249
T2	231	207	214	211	218	218	239	226	223	223
T3	221	201	206	204	210	210	228	217	214	214

Note. T1– (Cathelineau, 1988), T2– (Kranidiotis and McLenan, 1987), T3– (Kotelnikov et al., 2012)

Table 4. Summary of fluid inclusions data for sphalerite and quartz

Host mineral	n	T_{eut}, °C	T_m, °C	C, wt.%-NaCl eq.	T_{hom}, °C
Sphalerite	10	-28.0 … -24.3	-1.0 … -0.5	1.0 … 1.7	234 … 253
Quartz	14	-25.8 … -23.7	-3.6 … -2.5	4.0 … 5.8	205 … 246